CO_2 and Water Activation on Ceria Nanocluster Modified TiO_2 Rutile (110)

Stephen Rhatigan and Michael Nolan*

Tyndall National Institute, University College Cork, Lee Maltings, Cork, Ireland

*Corresponding author: michael.nolan@tyndall.ie

Abstract

Surface modification of TiO_2 with metal oxide nanoclusters is a strategy for the development of new photocatalyst materials. We have studied modification of TiO_2 rutile (110) with ceria nanoclusters using density functional theory corrected for on-site Coulomb interactions (DFT+U). We focus on the impact of surface modification on key properties governing the performance of photocatalysts, including light absorption, photoexcited charge carrier separation, reducibility and surface reactivity. Our results show that adsorption of the CeO_2 nanoclusters, with compositions Ce_5O_{10} and Ce_6O_{12}, is favourable at the rutile (110) surface and that the nanocluster-surface composites favour non-stoichiometry in the adsorbed ceria so that reduced Ce ions will be present in the ground state. The presence of reduced Ce ions and low coordinated O sites in the nanocluster lead to the emergence of energy states in the energy gap of the TiO_2 host, which potentially enhance the visible light response. We show, through an examination of oxygen vacancy formation, that the composite systems are reducible with moderate energy costs. Photoexcited electrons and holes localize on Ce and O sites of the supported nanoclusters. The interaction of CO_2 and H_2O is favourable at multiple sites of the reduced CeO_x-TiO_2 composite surfaces. CO_2 adsorbs and activates, while H_2O spontaneously dissociates at oxygen vacancy sites.

1 INTRODUCTION

Since the seminal paper by Fujishima and Honda in 1972,[1] titanium dioxide, TiO_2, has remained at the forefront of photocatalysis research due to its abundance, low-cost, non-toxicity and robustness under operating conditions. The large bandgap (>3 eV) means that TiO_2 is UV active so that extending light absorption to the visible range will potentially maximize solar energy absorption for large-scale implementation of photocatalytic technologies.

Strategies to induce visible light absorption in TiO_2 include substitutional cation or anion doping at Ti or O sites respectively[2-13] and co-doping, where multiple dopants are incorporated in the TiO_2 host.[12-20] Doping introduces impurity energy states into the bandgap of the TiO_2 host, facilitating electronic transitions with energies in the visible range. However, localized defect states can act as recombination centres, impeding carrier migration and reducing photocatalytic activity[9, 12, 13] and practical issues with reproducibility, solubility and stability persist with doped metal oxides.

Extending the absorption edge to longer wavelengths should not be the sole research focus; efficient separation of photoexcited charge carriers and molecular activation are essential to the performance of photocatalysts. The dye sensitized solar cell (DSSC)[21] can inspire similar strategies in photocatalysis; dyes simultaneously promote visible light absorption and charge separation but do suffer from degradation.[13] Noble-metal loading of TiO_2 has been reported to improve photocatalytic efficiency in the UV and the visible range through plasmon resonance in the metal.[22-26] However, the use of precious metals such as Ag, Au and Pt drives up costs.

Surface modification of TiO_2 with dispersed metal oxide nanoclusters of non-precious metals has been investigated experimentally via chemisorption-calcination cycle (CCC)[27, 28] and atomic layer deposition (ALD).[29] These studies reported both bandgap reduction and enhanced visible light photocatalytic activity for FeO_x-modified TiO_2. Photoluminescence spectroscopy

revealed that the modification suppressed carrier recombination[27] and the observed red shift was due to cluster derived states above the valence band maximum (VBM) as identified by X-ray photoelectron spectroscopy (XPS) and confirmed with density functional theory (DFT) simulations.[27, 28, 30]

DFT has been used in combination with experiment to examine these and similar systems.[28, 30-44] Our previous work[28, 31, 34-40, 43, 45] has indicated the potential for metal oxide modifiers to induce a bandgap reduction over bare TiO_2. We have also highlighted the role of low-coordinated nanocluster metal and/or oxygen sites in trapping and separating charge carriers[34, 36, 37, 40] and this suggests that modification of TiO_2 promotes electron and hole separation. Initial work on CO_2 activation at metal oxide modified TiO_2 has been presented.[31]

Transition metal oxides have been widely studied as catalysts for the oxygen evolution reaction (OER).[46, 47] A DFT study of water oxidation on rutile TiO_2 (110)[48] found that the most difficult step was H_2O dissociation at a vacancy site to form an adsorbed hydroxyl group (OH*). Other DFT studies examined water adsorption at extended surfaces of both rutile TiO_2 (110)[49] and CeO_2 (111)[50, 51] and found molecular adsorption to be more favourable than dissociative adsorption, albeit marginally so for the latter system (0.01-0.03 eV depending on exchange-correlation functional and separated by an energy barrier of 0.1 eV). A recent study compared water adsorption on TiO_2 anatase (101) (E_{ads} = -0.89 eV) and (001) (E_{ads} = -0.29 eV).[52] The authors attributed the greater activity of the (001) surface for water oxidation to hydrogen bonds between H_2O and terminal hydroxyls which facilitate rapid hole transfer. In general, the adsorption configuration of water molecules at TiO_2 surfaces depends on the crystal form, termination, stoichiometry and degree of coverage.[33, 53] However, an important first step, consistent across mechanisms describing water oxidation, is the dissociative adsorption of H_2O at the catalyst surface.[54-56] DFT+U studies examining Ce_2O_3 nanoclusters supported on rutile (110) found that water dissociation is exothermic (E_{ads} = -0.70 eV) with a small energy barrier

(0.04 eV).[42, 57] In addition, a number of studies have highlighted the role of dissociated H_2O, in particular surface hydroxyls, in trapping holes at catalyst surfaces,[52, 55, 58-60] which is important for subsequent steps in the water oxidation reaction.

The CO_2 reduction reaction (CO_2RR) competes with the hydrogen evolution reaction (HER) in the presence of water and in general H_2O adsorption at catalyst surfaces is preferential to CO_2 adsorption.[61] It is therefore necessary to promote selectivity for the desired reactions. DFT studies of CO_2 adsorption at titania surfaces ascribe a crucial role to oxygen vacancies in the activation process.[62, 63] Excess electrons and holes were shown to affect adsorption and activation of CO_2 at rutile (110),[64] with implications for binding energies, structure and reactivity of adsorbed CO_2; bent CO_2^- anion (excess electrons) and CO_2^+ cation (excess holes) configurations were identified. Sub-nm Pt clusters supported on anatase (101) enhanced CO_2 adsorption and activation through provision of additional adsorption sites at the edge of the Pt cluster;[65] transfer of electron density from the cluster to the TiO_2 substrate also facilitated adsorption at surface sites away from the supported Pt octamer.[65] Bismuth pyrochlore oxides have been shown to have a high CO_2 chemisorption capacity as identified through FTIR and attributed to the Bi_2O_3 motif with a Bi^{3+} lone pair.[66] Cu_2O has emerged as a potential candidate for CO_2RR due to its favourable bandgap position and width[67] and studies have focussed on the interaction of CO_2 molecules with various cuprous oxide surfaces and terminations.[67-72] A study of CO_2 adsorption at the Cu_2O (111): O terminated surface[70] found that adsorption at the perfect surface was more favourable by 0.15 eV than adsorption at the O deficient surface. The authors reported formation of a stable $CO_2^{\delta-}$ radical anion species upon adsorption at the O vacancy surface, but with an adsorption energy of ~0 eV. Another study examined the adsorption of CO_2 at Cu_2O (111) using Hybrid DFT[72] and found adsorption only in non-activated form. Physisorption of a linear CO_2 molecule is favoured over adsorption in activated form at Cu_2O (111),[68, 71] however strong chemisorption, with energy gains of as much as 1.76

eV, was reported for CO_2 adsorption at the Cu-O terminated (110) surface.[68] Activation, with bending and elongation of bonds, upon exothermic (E_{ads} = -0.96 eV) adsorption of CO_2 at CuO (011) has been reported.[69] Other theoretical studies examined reaction pathways involving the hydrogenation of CO and CO_2 at a variety of catalytic surfaces, including Cu/CeO_2 and $Cu/CeO_2/TiO_2$,[73] $Cu/ZnO/Al_2O_3$[74] and copper surfaces.[75, 76] Enhanced photoreduction of CO_2 with H_2O vapour has been reported for dispersed CeO_2 on anatase TiO_2, prepared using a one-pot hydrothermal method;[77] the role of Ce^{3+} in visible light absorption, photogenerated charge separation and strengthening CO_2-surface bonding was highlighted. The adsorption and activation of CO_2 at the catalyst surface is an important first step in subsequent reactions.

In this paper, we present a DFT study of heterostructures of TiO_2 rutile (110) modified with sub-nm nanoclusters of CeO_2. The clusters have compositions Ce_5O_{10} and Ce_6O_{12} and complement earlier work on Ce_2O_3 reduced nanoclusters supported on rutile (110).[42, 57, 79] CeO_2 is an interesting modifier as Ce 4f states are crucial in optical properties, reducibility and reactivity.[73, 77] The facile conversion between Ce^{4+} and Ce^{3+} oxidation states has important implications for catalytic performance and metal/CeO_x/TiO_2 composites with Ce^{3+} cations display enhanced activity for the water gas shift (WGS) reaction.[42, 57, 78, 79] We focus on the impact of nanocluster modification on (1) interfacial atomic structure, (2) valence or conduction band edges of rutile (110), (3) charge localization after excitation, (4) reducibility of the heterostructure and (5) interaction of feedstock molecules, H_2O and CO_2, with the reduced CeO_x-TiO_2 composite. A more reducible catalyst could use a combination of photocatalytic and thermal catalytic effects.[80] Electrons and holes can be produced by light absorption and thermally produced defects, such as oxygen vacancies, can provide sites for adsorption and activation of feedstock species.

We show that adsorption of ceria-nanoclusters at rutile (110) is favourable and that the nanocluster-surface composites favour non-stoichiometry so that reduced Ce ions will be

present in the ground state. Ce-derived occupied states emerge in the bandgap and low coordinated oxygen sites in the supported nanoclusters contribute to the density of states (DOS) at the TiO_2-derived VBM, potentially increasing the visible light response.

A photoexcitation model shows that the excited electron and hole localize onto the supported CeO_2 nanocluster. The interaction of CO_2 and H_2O is favourable at multiple sites of the reduced CeO_x-TiO_2 composite surfaces. H_2O spontaneously dissociates at oxygen vacancy sites to generate surface bound hydroxyls. Finally, CO_2 adsorbs and activates, forming a bent complex with elongated C-O distances.

2 METHODOLOGY

All calculations were performed using periodic plane wave density functional theory (DFT) as implemented in the VASP5.3 code.[81, 82] Valence electrons are described with a plane wave basis set with an energy cut-off of 396 eV. Projector augmented wave (PAW) potentials account for the core-valence electron interaction,[83, 84] with 4 valence electrons for Ti, 6 for O, 12 for Ce, 4 for C and 1 for H. The exchange-correlation functional is approximated by the Perdew-Wang (PW91) functional.[85]

Γ-point sampling is used for the (2×4) surface expansion of the rutile (110) surface with a supercell consisting of 18 monolayers (6 neutral trilayers) and a vacuum gap of 20 Å. The computed bulk lattice constants of rutile TiO_2 are $a = b = 4.64$ Å and $c = 2.97$ Å. The convergence criteria for the energy and forces are 10^{-4} eV and 0.02 eV Å^{-2} respectively. All calculations are spin polarized.

To consistently describe the partially filled Ti_{3d} and Ce_{4f} states a Hubbard U correction is applied.[86, 87] We use values of U(Ti) = 4.5 eV and U(Ce) = 5.0 eV with these values chosen

from previous work on CeO_2 and TiO_2.[37, 38, 40, 57, 88, 89] For calculations involving the model excited state and valence band hole formation we apply an additional +U correction to the O_{2p} state with U(O) = 5.5 eV. Previous work has highlighted the necessity for such a correction in obtaining a correctly localized oxygen hole state in metal oxides.[33, 35-37, 40] Aspherical gradient corrections are applied throughout and a dipole correction is used for the model excited state.

The ceria nanoclusters were adsorbed in different configurations at the rutile (110) surface which, in this work, is free of the point defects and surface hydroxyls which can be present on real surfaces.[90, 91] Relaxed atomic structures of the gas phase nanoclusters and their adsorption configurations at the rutile surface were determined as described in previous work[31-33, 35, 38, 43, 92] and further details are provided in the *Supporting Information*. The adsorption energies are computed using:

$$E_{ads} = E_{surf+A} - E_{surf} - E_A \quad (1)$$

where E_{surf+A}, E_{surf} and E_A are the energies of the adsorbate-surface composite system, the bare rutile (110) surface and the gas phase nanocluster respectively.

We examined reducibility *via* oxygen vacancy formation in the adsorbed CeO_2 nanocluster. One oxygen ion is removed from the adsorbed CeO_2 cluster and the vacancy formation energy is calculated as:

$$E_{vac} = E(Ce_xO_{y-1}) + 1/2E(O_2) - E(Ce_xO_y) \quad (2)$$

where the first and third terms on the right hand side are the total energy of the cluster-surface composite with and without an oxygen vacancy and the energy is referenced to half the total energy for molecular O_2. The calculation was performed for each oxygen site of the supported nanoclusters (see Table S1 *Supporting Information*) to determine the most stable non-stoichiometric composite. Once this is identified, we remove a second and third oxygen atom, as required, to describe situations in which multiple oxygen vacancies are present in the

nanocluster. Oxidation states were determined through Bader charge analysis[93] and computed spin magnetizations.

We investigated the adsorption and activation of H_2O and CO_2 at the CeO_2-modified rutile (110) composites, taking into particular account the presence of oxygen vacancies in CeO_2. Adsorption energies for molecules adsorbed at the nanocluster are calculated as:

$$E_{ads} = E_{surf+mol} - E_{surf} - E_{mol} \quad (3)$$

where $E_{surf+mol}$, E_{surf} and E_{mol} refer to the energies of the molecule and modified surface in interaction, the modified surface, and the gas phase molecule (H_2O or CO_2) respectively.

We model photoexcitation by imposing a triplet electronic state on the system.[94] This promotes an electron to the conduction band, with a corresponding hole in the valence band. We evaluate the energetics and charge localization associated with photoexcitation, as described in the *Supporting Information*.

3 RESULTS

3.1 Stoichiometric CeO_2-modified TiO_2 structures.

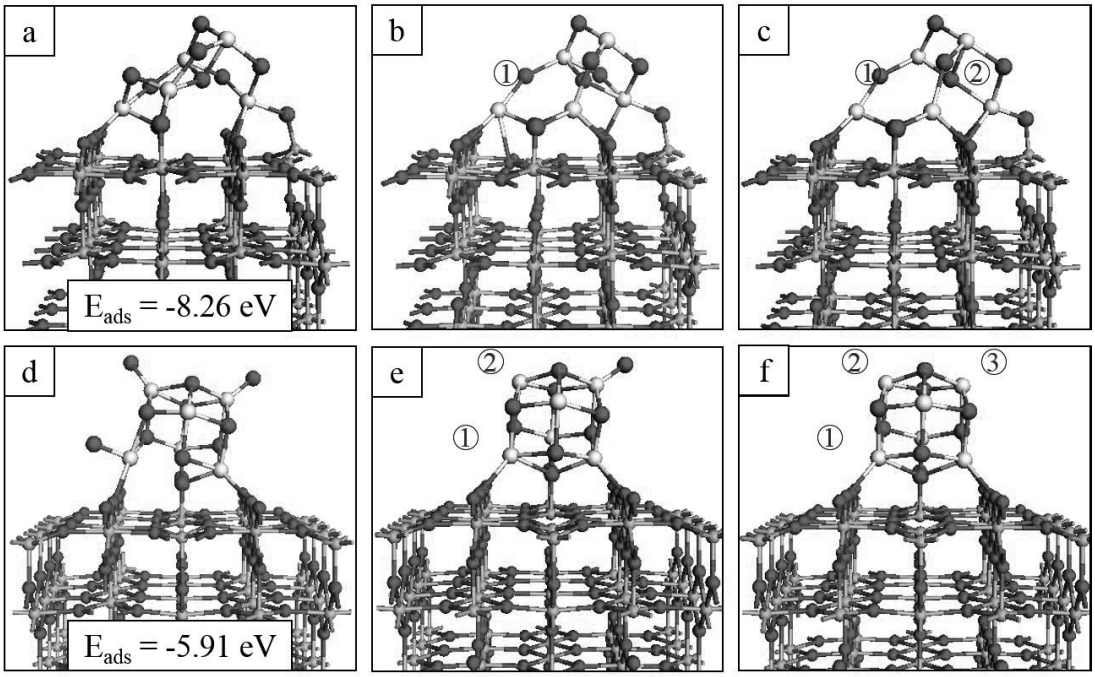

Figure 1. Top panels show the relaxed atomic structure of the Ce_5O_{10}-rutile-(110) composite in **(a)** stoichiometric form and after the formation of **(b)** one (ground state) and **(c)** two (reduced state) oxygen vacancies. Bottom panels show the atomic structure of the Ce_6O_{12}-rutile-(110) composite in **(d)** stoichiometric form and after the formation of **(e)** two (ground state) and **(f)** three (reduced state) oxygen vacancies. Insets of the left panels show the adsorption energies of the stoichiometric nanoclusters. The numbers in the black circles indicate the order in which oxygen atoms are removed from the nanocluster and are consistent with Table 1. In this and subsequent figures, Ti is indicated by a grey sphere, O by a red sphere and Ce by a cream sphere.

We focus on ceria nanoclusters of two compositions, Ce_5O_{10} and Ce_6O_{12}, and we first examine the stoichiometric nanocluster adsorption energies and structures shown in Figures 1(a) and 1(d). Adsorption energies were computed using Eq. 1 and are -8.26 eV for Ce_5O_{10} and -5.91 eV for Ce_6O_{12} adsorption on rutile (110). The negative adsorption energies show that

adsorption is favourable, with the magnitude of the energy indicating the strength of the interaction. From the adsorption energies we expect the nanoclusters to be stable at the surface without desorbing or migrating over the surface to form aggregates. Henceforth, the composites will be denoted as Ce_5O_x-rutile-(110) and Ce_6O_x-rutile-(110), where the subscript x will vary according to the stoichiometry. Oxygen atoms of the surface and nanocluster are distinguished by subscripts S and C respectively.

A detailed description of the local atomic structure at the nanocluster-surface interface is provided in the *Supporting Information*. Cerium ions show four-fold and five-fold coordination; the five-fold coordinated cations bind to O_S atoms. The nanocluster-surface interaction distorts the local atomic structure at the surface. Where a bridging O_S binds to a nanocluster cation the Ti-O_S distance is elongated by up to 10% compared with a typical unmodified Ti-O_S bond length of 1.88 Å. Titanium atoms that bind with O_C atoms migrate out of the surface plane towards the cluster by as much as 0.92 Å, lengthening the subsurface Ti-O_S distance.

3.2 Reduction of CeO_2-rutile by oxygen vacancy formation.

From the relaxed stoichiometric nanocluster-surface composites we remove O_C ions and compute the corresponding vacancy formation energies. Previous work on small CeO_2 structures on rutile (110) has shown that these prefer to be reduced, with loss of oxygen in the ground state, giving composition Ce_2O_3.[57, 73] It is not known if a similar composition would be found for larger but still sub-nm ceria clusters. The oxygen vacancy formation energies are important as their stability determines the stoichiometry of the composite. If the composite is then reduced, the formation energy can be a further important factor in determining if feedstock species will interact with the CeO_x-rutile composites. If the energy cost to form a reducing

vacancy is low, the system favours non-stoichiometry and fixation and activation of molecular species, *via* a redox or Mars van Krevelen process, may not occur and no reactions can take place. Conversely, while large vacancy formation energies can promote reoxidation *via* feedstock reduction, these require a large initial energy input and may also result in too strong interaction with molecular species, leading to poisoning of the surface.

Table 1 presents the computed oxygen vacancy formation energies in each supported ceria nanocluster; a full set of vacancy formation energies is presented in the *Supporting Information*. The most stable oxygen vacancy in Ce_5O_{10}-rutile-(110), which forms Ce_5O_9-rutile-(110), has a small cost of +0.02 eV so that the ground state is off-stoichiometric. For a second oxygen vacancy, to give Ce_5O_8-rutile-(110), the most stable vacancy site has an energy cost of +1.33 eV, relative to Ce_5O_9-rutile-(110). Thus the second oxygen vacancy is the reducing oxygen vacancy and this has a moderate cost.

For Ce_6O_{12}-rutile-(110), the first two oxygen vacancies have negative formation energies, of -0.26 eV and -0.62 eV, and will form spontaneously at T = 0 K; the ground state is highly off-stoichiometric, with composition Ce_6O_{10}-rutile-(110). This instability of the stoichiometric composite sheds light on the small adsorption energy of Ce_6O_{12} relative to Ce_5O_{10}. The energy cost required to produce the most stable third oxygen vacancy, giving Ce_6O_9-rutile-(110), is +0.31 eV. This cost is moderate and we consider the Ce_6O_9-rutile-(110) composite as being in a reduced state. Thus, for rutile modified by a sub-nm ceria nanocluster, we expect a highly non-stoichiometric system with multiple potential activation sites at moderate temperatures, consistent with the work of Graciani *et al.*[73]

Table 1 Computed oxygen vacancy formation energies in CeO_2-rutile composites. The values listed correspond to the most stable configuration after removal of one, two or three oxygen atoms in the cluster and correspond to the numbering in Figure 1.

Reaction	**Oxygen vacancy**	**Formation energy (eV)**
$Ce_5O_{10} \rightarrow Ce_5O_9$	$E_{vac,1}$	+0.02
$Ce_5O_9 \rightarrow Ce_5O_8$	$E_{vac,2}$	+1.33
$Ce_6O_{12} \rightarrow Ce_6O_{11}$	$E_{vac,1}$	-0.26
$Ce_6O_{11} \rightarrow Ce_6O_{10}$	$E_{vac,2}$	-0.62
$Ce_6O_{10} \rightarrow Ce_6O_9$	$E_{vac,3}$	+0.31

Figure 1 shows the atomic structures of the non-stoichiometric ground state (1(b) and 1(e)) and reduced (1(c) and 1(f)) nanocluster-surface composites; black circles in the images indicate the site number of the removed oxygen, corresponding to Table 1.

After formation of the first oxygen vacancy in Ce_5O_{10}-rutile-(110), the two Ce ions which were bound to this oxygen maintain their coordination by binding to O_S atoms (Figure 1(b)). In total, three new nanocluster-surface bonds are formed, two involving bridging O_S and the third involving an in-plane O_S which migrates out from the surface by 0.1 Å. One Ce-O_S bond is broken during the relaxation; the coordination of the Ce is maintained by binding to the central O_C atom with the latter now four-fold coordinated. After formation of the second vacancy, yielding Ce_5O_8-rutile-(110) (Figure 1(c)), one Ce ion is three-fold coordinated, while the remaining Ce are four- and five-fold coordinated. In both the ground state, with one O vacancy, and the reduced composite, with two O vacancies, there are nine interfacial bonds, up from seven in the stoichiometric Ce_5O_{10}-rutile-(110) composite.

For Ce_6O_{12}-rutile-(110), the formation of oxygen vacancies to produce the ground state, Ce_6O_{10}-rutile-(110) (Figure 1(e)), and reduced, Ce_6O_9-rutile-(110) (Figure 1(f)), composites has no impact on the number of interfacial bonds. However, the Ce ions to which the removed terminal O atoms were bound, relax towards the nanocluster, increasing their coordination by binding to other O_C atoms.

In these non-stoichiometric nanocluster-surface composites we expect to find two electrons released for each neutral oxygen vacancy and spin density plots are used to determine the location of the electrons after relaxation. Spin density plots for the ground and reduced states of CeO_x-rutile are presented in Figure 2. Electron localization occurs at Ce atoms in each nanocluster, which results in the formation of reduced Ce^{3+} cations. Ce^{3+} form in preference to Ti^{3+} cations, as also reported in DFT+U studies of Ce-doped TiO_2[95-97] and some surfaces.[42, 79]

For the non-stoichiometric ground states, with compositions Ce_5O_9-rutile-(110) and Ce_6O_{10}-rutile-(110), two and four Ce atoms are reduced as shown in Figures 2(a) and 2(c). When the composites are reduced, giving compositions Ce_5O_8-rutile-(110) (Figure 2(b)) and Ce_6O_9-rutile-(110) (Figure 2(d)), four and six Ce atoms are reduced respectively.

These results are confirmed through Bader charge analysis, shown in Table 2. Typical net atomic charge values for Ce^{4+} ions are in the range of 9.6 to 9.8 electrons for the stoichiometric nanoclusters. Upon oxygen vacancy formation and the subsequent localization of excess spin on Ce atoms, the net atomic charges increase by 0.2 electrons for reduced cations; this is typical for $Ce^{4+} \rightarrow Ce^{3+}$ reduction. The computed spin magnetizations for reduced Ce^{3+} cations are 0.97-0.98 μ_B.

In general, Ce-O distances involving Ce^{3+} species are elongated by 0.1-0.2 Å due to the larger ionic radius of Ce^{3+} compared to Ce^{4+}; this effect is less strong in cases where the reduced Ce ions have a lower coordination or where the Ce ion was previously bound to a singly

coordinated O atom. See Table S2 in the *Supporting Information* for details of the Ce-O distances in each case.

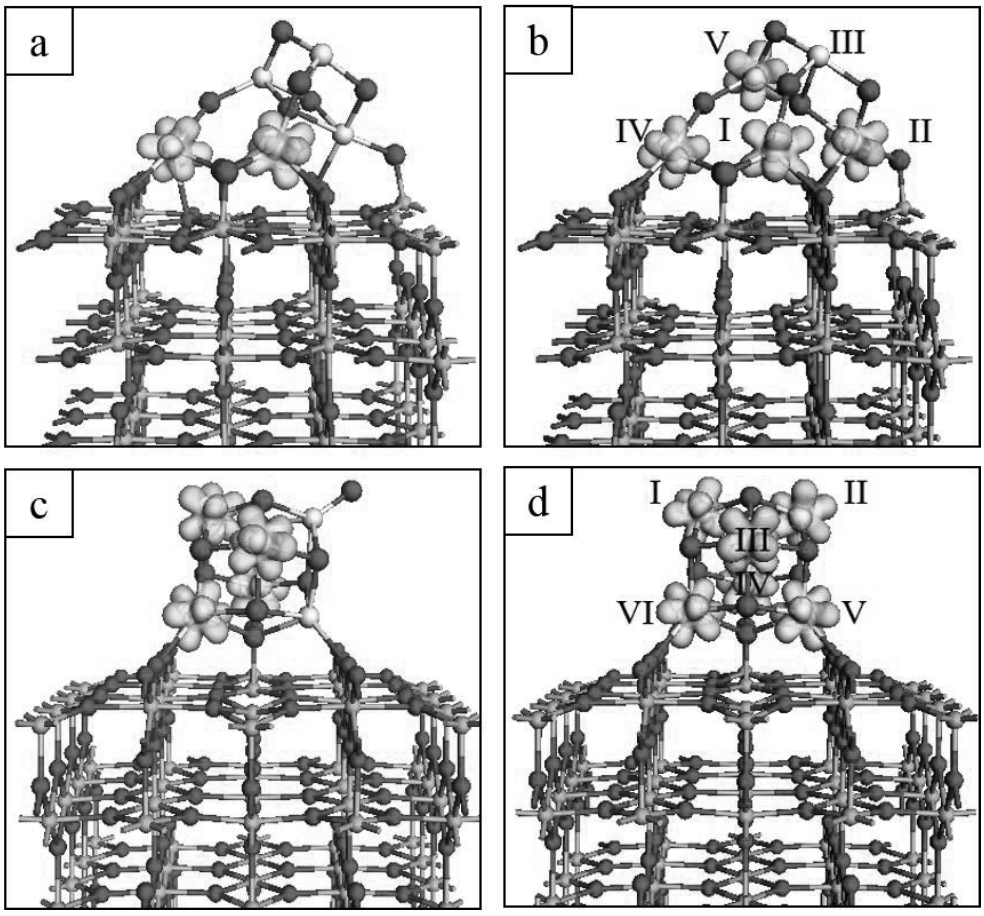

Figure 2. Excess spin density plots for Ce_5O_{10}-modified rutile (110) with **(a)** one (ground state) and **(b)** two (reduced) oxygen vacancies and Ce_6O_{12}-modified rutile (110) with **(c)** two (ground state) and **(d)** three (reduced) oxygen vacancies. The spin density isosurfaces are yellow and enclose spin densities of up to 0.2 eV/Å^3. The roman numerals in the panels on the right hand side correspond with the labelling in Table 2.

Table 2 Computed Bader charges for the cerium ions in the supported nanoclusters before and after formation of one or more oxygen vacancies. Superscripts [a], [b], and [c] denote the stoichiometric, off-stoichiometric ground state, and reduced nanocluster-surface composites respectively. Reduced Ce^{3+} are highlighted in bold.

	$^{a}Ce_5O_{10}$	$^{b}Ce_5O_9$	$^{c}Ce_5O_8$		$^{a}Ce_6O_{12}$	$^{b}Ce_6O_{10}$	$^{c}Ce_6O_9$
Ce_I	9.6	**9.9**	**9.9**	Ce_I	9.7	**10.0**	**10.0**
Ce_{II}	9.6	9.6	**9.9**	Ce_{II}	9.7	9.8	**10.0**
Ce_{III}	9.8	9.8	9.8	Ce_{III}	9.8	**10.0**	**10.0**
Ce_{IV}	9.7	**9.9**	**9.9**	Ce_{IV}	9.7	**9.9**	**9.9**
Ce_V	9.7	9.7	**10.0**	Ce_V	9.7	9.7	**9.9**
				Ce_{VI}	9.7	**9.9**	**9.9**

The spin polarized projected electronic density of states (PEDOS) for the stoichiometric, off-stoichiometric ground state and reduced nanocluster-surface composites are presented in Figure 3. Figures 3(a) and 3(d) show the stoichiometric configurations where the most obvious feature is the presence of states at the top of the VB for the Ce_6O_{12} nanocluster. These states are due to singly coordinated O_C ions (see Figure 1(d)). However, nanocluster-derived oxygen 2p states above the TiO_2 VB persist even after removing these oxygen sites. Figures 3(b), 3(c), 3(e) and 3(f), which correspond to the off-stoichiometric CeO_x-rutile composites, new states emerge in the TiO_2-derived bandgap, due to the singly occupied $4f^1$ orbital configuration of reduced Ce^{3+} cations in the oxygen deficient nanoclusters. Modification of rutile with CeO_x nanoclusters will result in a red shift of the TiO_2 adsorption edge; this is due to a combination of 2p states of low coordinated O_C sites pushing the VBM to higher energy and the emergence of mid-gap states associated with reduced Ce^{3+} ions in the off-stoichiometric composites. Absorption spectra were computed for unmodified rutile (110) and for the ground state

composites, Ce_5O_9- and Ce_6O_{10}-rutile-(110) and are shown in Figure S3 of the *Supporting Information*. The results show a red shift in the adsorption edge due to modification and corroborate the analysis of the DOS plots.

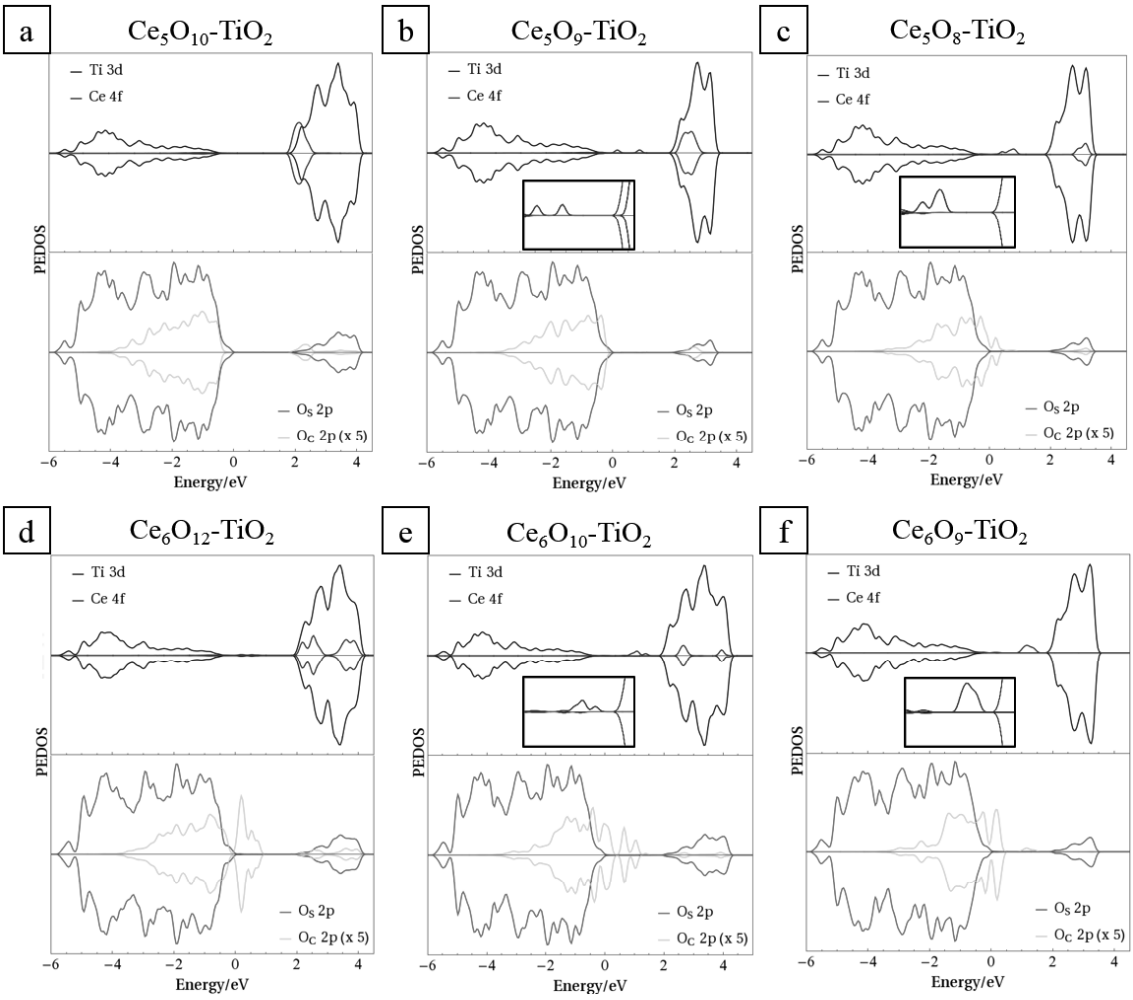

Figure 3. Spin polarized projected electron density of states (PEDOS) for **(a)** Ce_5O_{10}-, **(b)** Ce_5O_9-, **(c)** Ce_5O_8-, **(d)** Ce_6O_{12}-, **(e)** Ce_6O_{10}- and **(f)** Ce_6O_9-rutile-(110). The top half of each panel displays Ti 3d- and Ce 4f-derived states. Bottom halves of the panels display contributions to the DOS from surface (O_S) and nanocluster (O_C) oxygen 2p-derived states. Insets in the top panels show the mid-gap Ce-derived states in the range [-0.25 eV, + 2.25 eV].

3.3 Modelling charge separation upon photoexcitation.

We apply the photoexcited model to the ground state systems, Ce_5O_9-rutile-(110) and Ce_6O_{10}-rutile-(110). Table 3 presents the computed vertical, singlet-triplet and the electron-hole localization (relaxation) energies, as discussed in the *Supporting Information*. First, we note the underestimation of the bandgap inherent in approximate DFT is present in our DFT+U computational set-up. The +U corrections used herein are chosen to consistently describe the localization of electrons and holes rather than to reproduce the bandgap of bulk TiO_2, which is not advised. This underestimation is clear in the computed values for $E^{vertical}$ and E^{excite} which are smaller than experimental values. However, comparison of these computed energies across different structures yields useful qualitative information about the effect of surface modification. In particular, a reduction in E^{excite} for a composite structure relative to the unmodified metal oxide will correspond to a red shift in light absorption for the surface modified system.

Table 3 Vertical singlet-triplet energy difference ($E^{vertical}$), the relaxed singlet-triplet energy difference (E^{excite}) and the relaxation energy (E^{relax}) for nanocluster rutile (110). Values for unmodified rutile (110) have been included for reference.

Composite structure	**$E^{vertical}$ (eV)**	**E^{excite} (eV)**	**E^{relax} (eV)**
Bare-rutile (110)	2.02	1.97	0.05
Ce_5O_9-rutile (110)	1.76	0.96	0.80
Ce_6O_{10}-rutile (110)	1.30	0.51	0.80

We note that E^{excite} is always smaller than $E^{vertical}$ and the simple VB-CB energy difference, as the former includes ionic relaxations and polaron formation in response to "exciting" the electron, which stabilize the triplet electronic state. The energies presented in Table 3 show

that modification of rutile (110) with CeO_2 nanoclusters leads to a red shift in light absorption whether we use the vertical or excitation energies. This effect is stronger for the larger nanocluster, consistent with the PEDOS. Relaxation energies of 0.8 eV upon charge localization in each heterostructure indicate high stability of the photogenerated electron-hole pairs.

We can also examine the localization of the electron-hole pair through analysis of computed Bader charges, spin magnetizations and excess spin density plots. Figure 4 shows the spin density plots for Ce_5O_9-rutile-(110) after relaxation of the triplet state; electrons are shown in yellow and holes in blue. Spin density plots and analysis for the excited state model applied to Ce_6O_{10}-rutile-(110) can be found in the *Supporting Information*. Since the modifier is off-stoichiometric in the ground state, reduced Ce^{3+} ions are present prior to imposing the excited state. For Ce_5O_9-rutile-(110), shown in Figure 4, there are three unpaired electrons; two are due to the neutral oxygen vacancy and are localized at Ce_I and Ce_{IV} (compare with Figure 2(a)). The third electron is the photoexcited electron and is localized on Ce_{II}; this Ce ion, which was five-fold coordinated in the ground state, is four-fold coordinated after localization of the photoexcited electron and the Ce-O bonds are elongated by as much as 10%. Electron localization at the Ce ion increases the computed Bader charge by 0.2 electrons, similar to the trend presented in Table 2, and the computed spin magnetizations are 0.97 μ_B.

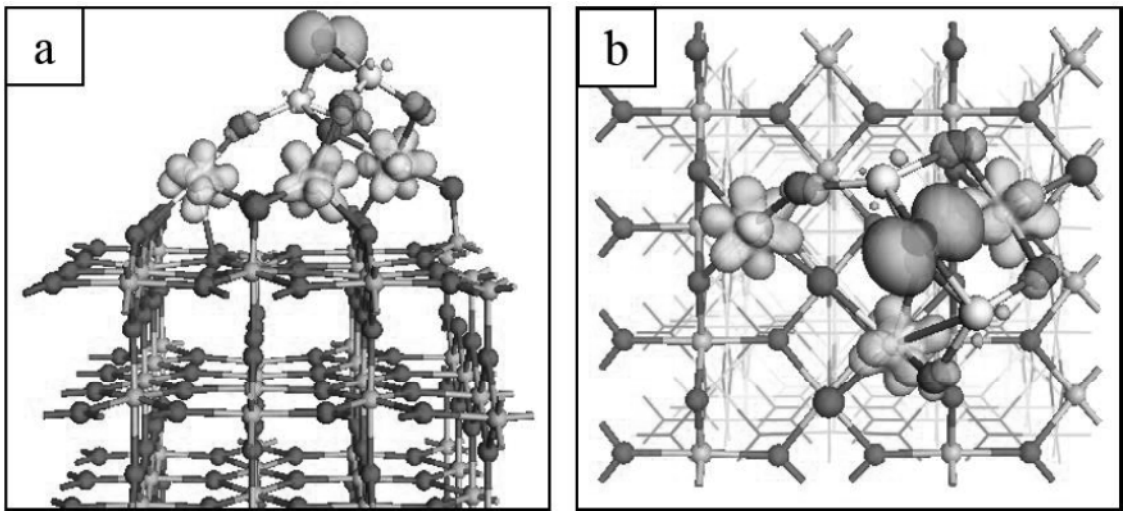

Figure 4. Spin density plots for the photoexcited electron and hole in Ce_5O_9-rutile-(110) for **(a)** side and **(b)** top view. The spin density isosurfaces are yellow for electrons and blue for holes and enclose spin densities of up to 0.02 eV/Å^3.

The hole predominantly localizes on a single, low-coordinated O_C site, shown in blue in Figure 4. For Ce_5O_9-rutile-(110), the oxygen site at which the hole predominantly localizes is two-fold coordinated both before and after photoexcitation; the Ce-O distances increase from 2.1 Å in the ground state to 2.4 Å in the excited state. Hole localization is accompanied by a change in the computed Bader charge of the oxygen from 7.1 to 6.7 electrons. There is some spreading of the hole to neighbouring two-fold coordinated O_C sites. This is typical for this DFT+U set-up and is accompanied by changes of < 0.1 electrons in the computed Bader charges; we can conclude the hole predominantly localizes on one O_C site. This is confirmed by a computed spin magnetization of 0.73 μ_B for the oxygen hole on Ce_5O_9-rutile-(110).

For the CeO_x-rutile-(110) composites, both the electron and hole localize on the nanocluster modifiers, which may have consequences for recombination. However, the spatial separation of the charges is maximal (see Figures 4 and S4), given that both electrons and holes localize

at nanocluster sites. In addition, the large relaxation or trapping energies act to impede migration of the charges and thus the impact on recombination should be minor. We note that this photoexcited model, which imposes a triplet state to induce a transition from the VB to the CB, precludes transitions from the highest occupied, Ce 4f-derived states of the off-stoichiometric ground states (see Figures 3(b) and 3(e)). Such transitions amount to electron hopping between Ce sites of the nanocluster with no change in electronic configuration after "excitation". Rather, our model with a triplet electronic state (in addition to the unpaired electrons on reduced Ce^{3+}) will induce transitions from O_C 2p-derived states, which sit at the top of the titania-derived VB, to the unoccupied Ce 4f states.

3.4 H_2O adsorption at the reduced nanocluster-surface composites.

We examined how water interacts at vacancy sites in the reduced CeO_x-rutile-(110) composites and computed the adsorption energies using Eq. 2. Water adsorption is favourable at multiple sites on the supported CeO_x nanoclusters. Adsorption energies for the most stable adsorption configurations of water are -1.79 eV on Ce_5O_8-rutile-(110) and -1.09 eV on Ce_6O_9-rutile-(110); the corresponding geometries are displayed in Figure 5. Figure S5 in the *Supporting Information* shows additional adsorption sites and energies for the H_2O-CeO_x-TiO_2 interaction.

Starting from an initial water adsorption in molecular form, the most stable adsorption mode is that in which the water molecule dissociates spontaneously upon relaxation. This dissociation involves the transfer of an H atom to an O_C site and the hydroxyl from the water molecule bridges two cluster Ce sites. For Ce_6O_9-rutile-(110), the moderate adsorption energy means that hydroxyls should not be over-stabilized and could be active in catalysis. Thus, water dissociation and activation can be promoted on these ceria-rutile composites.

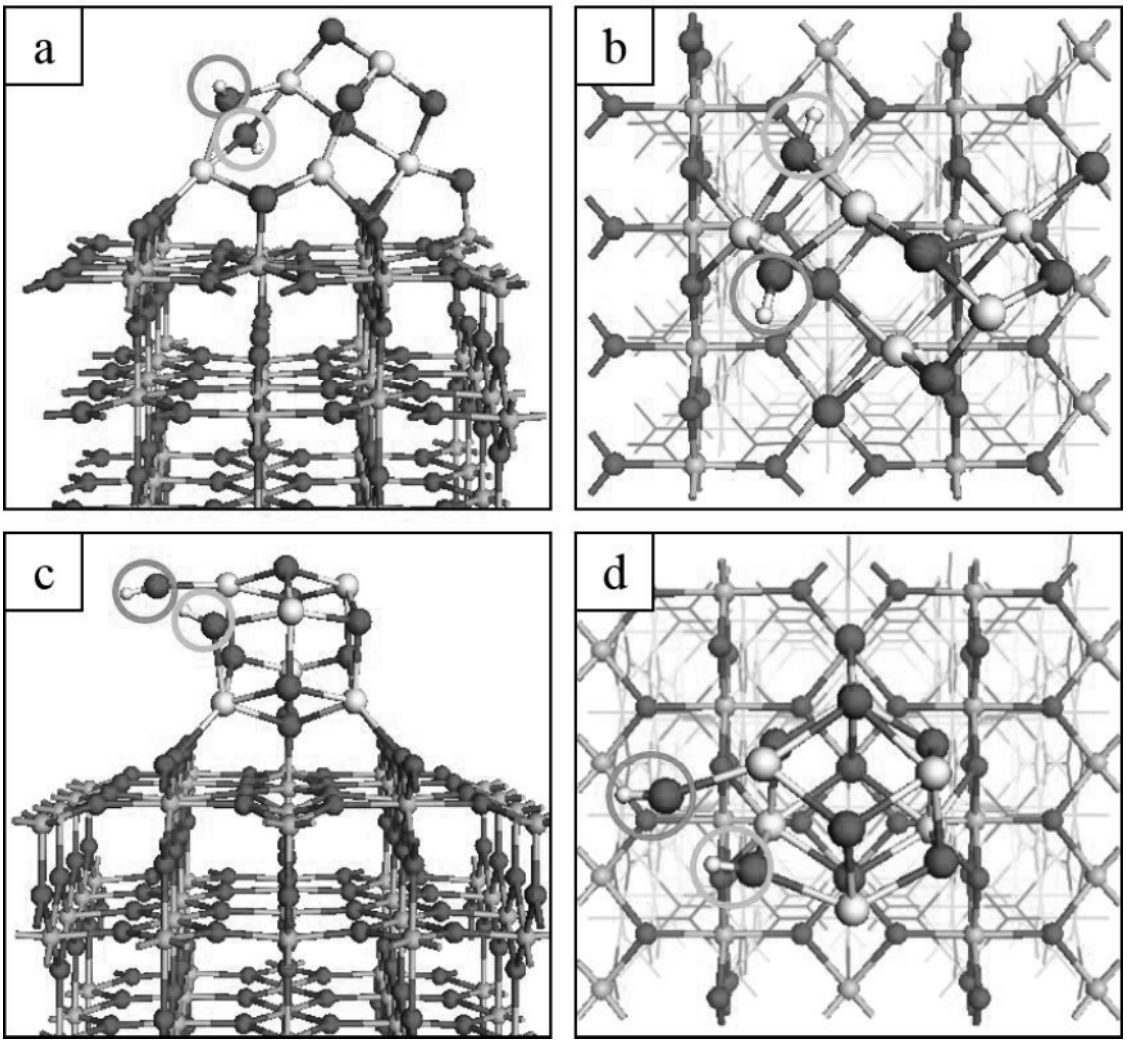

Figure 5. Relaxed atomic structures of the most stable configurations of H_2O adsorbed at **(a)** and **(b)** Ce_5O_8-rutile-(110) and **(c)** and **(d)** Ce_6O_9-rutile-(110). Hydroxyl groups arising from the spontaneous dissociation at the surface are circled in blue for the water-derived OH and in orange for the OH involving O_C sites. H atoms are represented by small white spheres.

For adsorption of water at Ce_5O_8-rutile-(110) (Figures 5(a) and 5(b)), the water molecule interacts with low-coordinated cluster sites. The OH group fills a vacancy site (O_1 from Figure 1(b)), and binds to two Ce^{3+} sites which were four- and three-fold coordinated; the latter being the lowest coordinated cluster cation. The second H atom transfers to a two-fold coordinated O_C site which neighbours the Ce sites bound to the hydroxyl and is among the lowest-

coordinated O_C sites. Ce-O bond lengths involving both cluster- and water-derived OH groups are elongated by up to 0.3 Å, relative to equivalent Ce-O distances prior to water adsorption. Bader charge analysis reveals that there is no charge transfer between the nanocluster and water and no Ce^{3+} cations are reoxidized. There is a charge redistribution, with an increase in charge of 0.3 electrons in the nanocluster as a result of formation of hydroxyls, which is predominantly transferred to the O_C that binds with hydrogen. A description of the dissociative adsorption of water at Ce_6O_9-rutile-(110), which is qualitatively similar to adsorption at Ce_5O_8-rutile-(110), including local atomic structure and Bader charge analysis is provided in the *Supporting Information.*

These results compare with studies of water dissociation at Ce_2O_3-TiO_2.[57, 98] In these studies the authors followed the energy pathway from water adsorbed in molecular form to dissociation, finding that the dissociation process was exothermic (-0.70 eV) with a small energy barrier of 0.04 eV. We found that dissociation of molecular water occurred spontaneously, suggesting that the size of the supported CeO_x nanocluster and the number of Ce^{3+} sites play a role in the ability of the composite to dissociate water.

While the ability of metal oxides to dissociate H_2O is well established, the mechanism which promotes dissociation remains of interest. A number of studies have looked at CeO_2 surfaces as model systems to study water dissociation.[99-102] Defects, step edges and terraces in surfaces play a role as such features provide low-coordinated adsorption sites. CeO_2 (111) with O vacancies and Ce^{3+} ions shows a preference for dissociative water adsorption, relative to the pristine surface, where there is little energetic difference between adsorption in molecular and dissociated form.[103] Similar results were found for CeO_2 (111);[104] the presence of O vacancies made dissociative adsorption more favourable, by 1.1 eV relative to molecular water, with no energy barrier. The authors also found that Ni and Ni_4 at the surface introduced Ce^{3+} ions and had a moderating effect on the water adsorption energies; for Ni/CeO_2(111), dissociation was

favoured by 0.3 eV with a small energy barrier of 0.13 eV. High lying 2p states, derived from low coordinated O_C sites, with the presence of Ce^{3+} states in the gap, facilitates interactions with water to break O-H bonds. A recent study showed that increased lattice strain in the CeO_2 (111) surface promotes dissociation of H_2O over molecular adsorption.[105] For the reduced Ce_6O_9-rutile-(110) composite, the Ce-O distances, at the sites of H_2O adsorption (see Figures 5(c) and 5(d)), are longer by ~1% relative to typical distances (~2.37 Å) in the pristine CeO_2 (111) surface. This suggests that tensile strain may indeed contribute to promoting the dissociation of water. In Ce_5O_8-rutile-(110), Ce-O distances are shorter (~2.2 Å), due to the lower coordination of the O_C sites, and elongate after the dissociative adsorption of H_2O. However, the Ce-Ce distance prior to water adsorption is 4.2 Å, which is considerably longer than neighbouring Ce-Ce distances (~3.9 Å) in CeO_2 (111). After dissociative adsorption of water, this Ce-Ce distance decreases to 3.6 Å, further indicating that tensile strain may play a role in driving dissociation.

Figure 6 shows the PEDOS of the H_2O molecule and reduced Ce_5O_8-rutile-(110) composite in the non-interacting case (H_2O + surface) and after dissociative adsorption (H_2O-surface). Similar analysis is provided for Ce_6O_9-rutile-(110) in Figure S6 of the S*upporting Information*. For the non-interacting system the molecule and surface are relaxed in the same unit cell with sufficient spatial separation such that they do not interact. In the non-interacting case (Figure 6(a)), the water-derived O_W 2p states show well defined peaks at energies of -2.9 eV and -0.8 eV relative to the VBM (0 eV) of the TiO_2 support. For the interacting case (Figure 6(b)) the O_W 2p-derived states overlap the O_C 2p-derived states near the VBM of the titania host. For water adsorbed at Ce_5O_8-rutile-(110), the O_W 2p states broaden and lie below the VBM, overlapping with O_C derived states, as the OH groups each bridge two Ce sites of the nanocluster. Comparing Figures 6(a) and 6(b), the O_W-derived states are shifted to lower energies upon dissociative adsorption.

The interaction increases the gap between the occupied Ce 4f-derived states and the CBM of the TiO_2 host (see insets of panels in Figure 6); i.e. the occupied Ce^{3+} states are pushed to lower energy after interaction. In addition, integrating the O_C and O_W-derived DOS lying above the TiO_2 VBM in both the non-interacting and interacting cases shows that after interaction the occupied states are driven to lower energies. The number of states lying above the TiO_2 VBM is reduced by 2 in the interacting case relative to the non-interacting system; this suggests that passivation of high lying O 2p states is a factor driving the interaction of water with the reduced CeO_x-rutile-(110) composite surfaces.

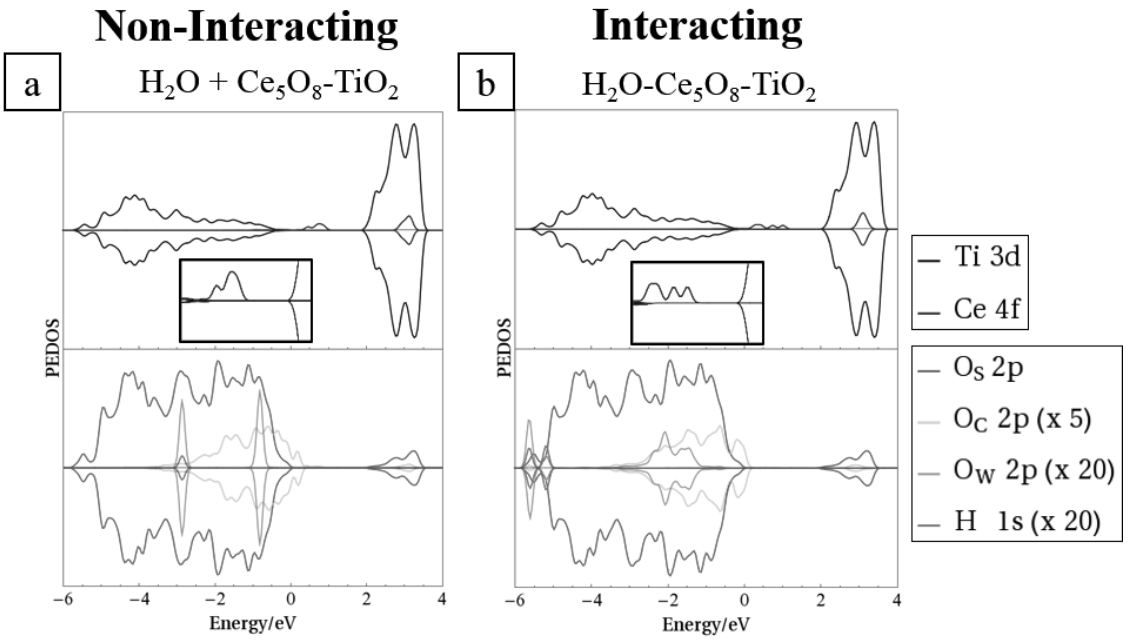

Figure 6. Spin polarized projected electron density of states (PEDOS) for **(a)** $H_2O + Ce_5O_8$-rutile-(110) (non-interacting) and **(b)** H_2O-Ce_5O_8-rutile-(110) (interacting). The top half of each panel displays Ti 3d- and Ce 4f-derived states. Bottom halves of the panels display contributions to the DOS from surface (O_S), nanocluster (O_C) and water (O_W) oxygen 2p-derived states and H 1s states. Insets in the top panels show the mid-gap Ce-derived states in the range [-0.25 eV, +2.25 eV].

3.5 CO_2 adsorption at the reduced nanocluster-surface composites.

With the motivation that O vacancies in reduced metal oxides can act as sites for the adsorption and activation of CO_2, as found in other studies,[70, 106-109] we examined CO_2 adsorption at various sites on reduced Ce_5O_8- and Ce_6O_9-rutile-(110); the computed adsorption energies for the most stable configurations are -1.20 eV on Ce_5O_8-rutile-(110) and -1.25 eV on Ce_6O_9-rutile-(110). The relaxed geometries for these configurations are shown in Figure 7. Figure S7 in the *Supporting Information* shows additional adsorption structures and energies for the CO_2-CeO_x-TiO_2 interaction.

The negative adsorption energies and their magnitudes indicate a strong exothermic interaction between CO_2 and the oxides. Our results follow the trend that CO_2 interaction is stronger at vacancy sites with a higher formation energy, as previously reported.[31] A DFT+U study of CO_2 activation on CeO_2 (110) found that the most stable O vacancy had a formation energy of +1.65 eV;[110] the authors reported that CO_2 adsorption at this site, with a bent geometry and E_{ads} = -1.22 eV, was the most stable adsorption configuration. A DFT+U study of CO_2 reduction on CeO_2 (111) also found that interaction was strongest at the O-defective surface;[111] the O vacancy formation energy was +2.78 eV and CO_2 adsorbed in a bent geometry with E_{ads} = -1.12 eV. While the adsorption energies are comparable across these studies, the vacancy formation energy is not sufficient in predicting the strength of interaction of adsorbed CO_2. Previous work on Ce_3O_6-rutile-(110)[31] found that this composite was reducible with an O vacancy formation energy of +0.31 eV; CO_2 was calculated to adsorb exothermically with E_{ads} = -0.20 eV. This compares with an adsorption energy of -1.25 eV for CO_2 interacting at the reduced Ce_6O_9-rutile-(110) composite of the present work in which oxygen vacancies are produced with similar energy costs (see Table 1). This suggests that, in the case of ceria nanocluster modifiers, the degree of non-stoichiometry, which is related to the number of reduced Ce cations in the cluster, may play a role in stabilizing adsorbed surface species. Future

work, involving larger ceria nanocluster modifiers, can shed further light on the nature of the trade-off between interaction strength and reducibility.

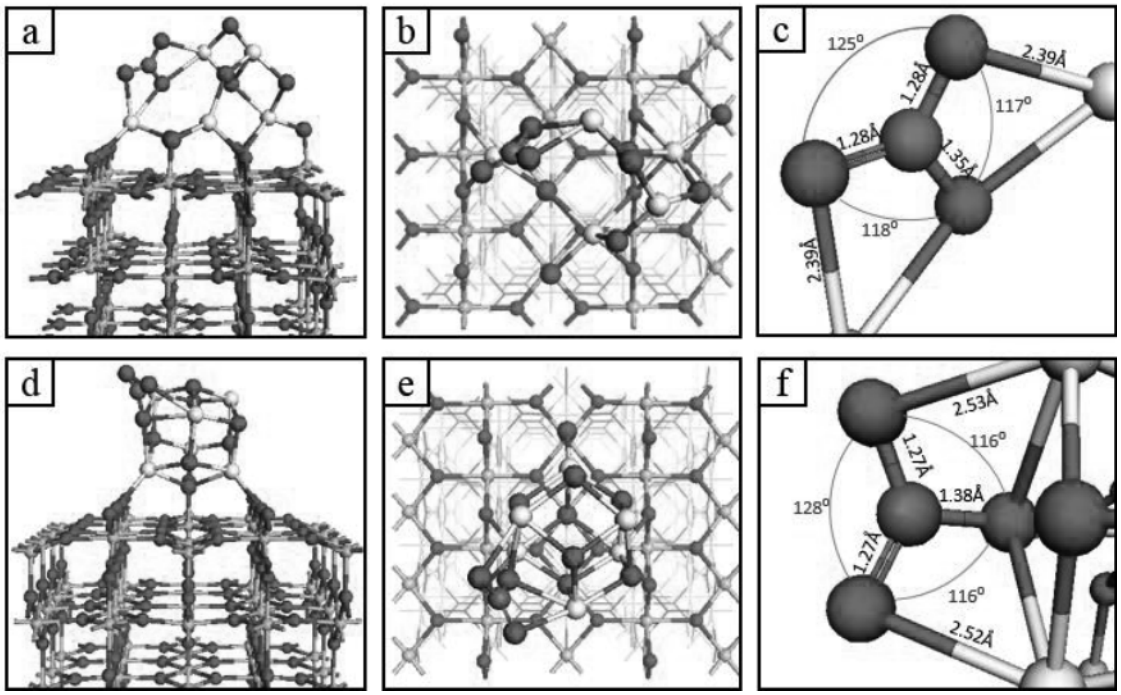

Figure 7. Relaxed atomic structure for most stable configurations of CO_2 adsorbed at **(a)**, **(b)** and **(c)** Ce_5O_8-rutile-(110) and **(d)**, **(e)** and **(f)** Ce_6O_9-rutile-(110). **(a)**, **(d)** Side views; **(b)**, **(e)** top views and **(c)**, **(f)** key geometry data around the CO_2 adsorption site. Carbon atoms are indicated by dark grey spheres.

The relaxed structures of the most stable configurations of CO_2 adsorbed at the CeO_x-TiO_2 heterostructures are similar across both nanocluster modifiers and all sites. Adsorption favours formation of an activated CO_2 complex which has two elongated C-O bonds in the adsorbed CO_2 molecule and a third, longer C-O bond involving an O_C near the adsorption site. This results in a surface bound species with the binding further strengthened by the interaction of the oxygen atoms of CO_2 and Ce cations in the nanoclusters.

The O-C-O angle of adsorbed CO_2 is in the range of 125-128^0, depending on the adsorption site; the two O-C-O angles involving O_C are in the range of 115-118^o. This deviation of the O-C-O angle from 180^o in the linear gas phase CO_2 is a key signature of CO_2 activation, as discussed on other systems.[112-114] C-O distances in adsorbed CO_2 are 1.26-1.28 Å with the C-O_C bond length in the range of 1.35-1.39 Å. Thus, the C-O bonds in adsorbed CO_2 are significantly elongated over the gas phase (C-O ≈ 1.16 Å), coupled with considerable bending of the O-C-O bond angle. This means that the interaction leads to an activated, chemisorbed CO_2 species and the formation of an inactive, strongly bound carbonate species can be ruled out.

The Ce-O bonds established with the adsorbed species are comparable in length to those within the nanocluster, which are 2.2-2.6 Å. The calculated Bader charges show that charge transfer is consistent across the various adsorption sites. Between 0.1 and 0.2 electrons are transferred from the CO_2-derived O atoms to the cluster, while the O_C at the adsorption site gains between 0.4 and 0.6 electrons through the interaction.

The PEDOS for CO_2 and reduced Ce_5O_8-rutile-(110) heterostructures in the non-interacting case and after CO_2 adsorption and activation are shown in Figure 8. Similar analysis is provided for Ce_6O_9-rutile-(110) in Figure S8 of the S*upporting Information*. In the non-interacting case, the CO_2 molecule-derived O_M 2p states show well defined peaks at energies of -7.2 eV and -3.7 eV (Figure 8(a)) relative to the VBM (0 eV). The highest occupied molecular orbital (HOMO) of the CO_2 molecule coincides with the deepest levels of the ceria nanocluster-derived VB. This alignment of O_M 2p and O_C 2p states can, in part, facilitate the interaction of CO_2 with the modified surface. The high lying O_C 2p states of the heterostructure can enhance the basic character of supported CeO_x. Wu *et al* showed that ceria nanoshapes, which support multiple defects, display a strong basic character that promotes CO_2 adsorption.[115] Thus, it is

reasonable to propose that the defective, supported ceria nanoclusters will also show enhanced basicity and thus promote CO_2 adsorption.

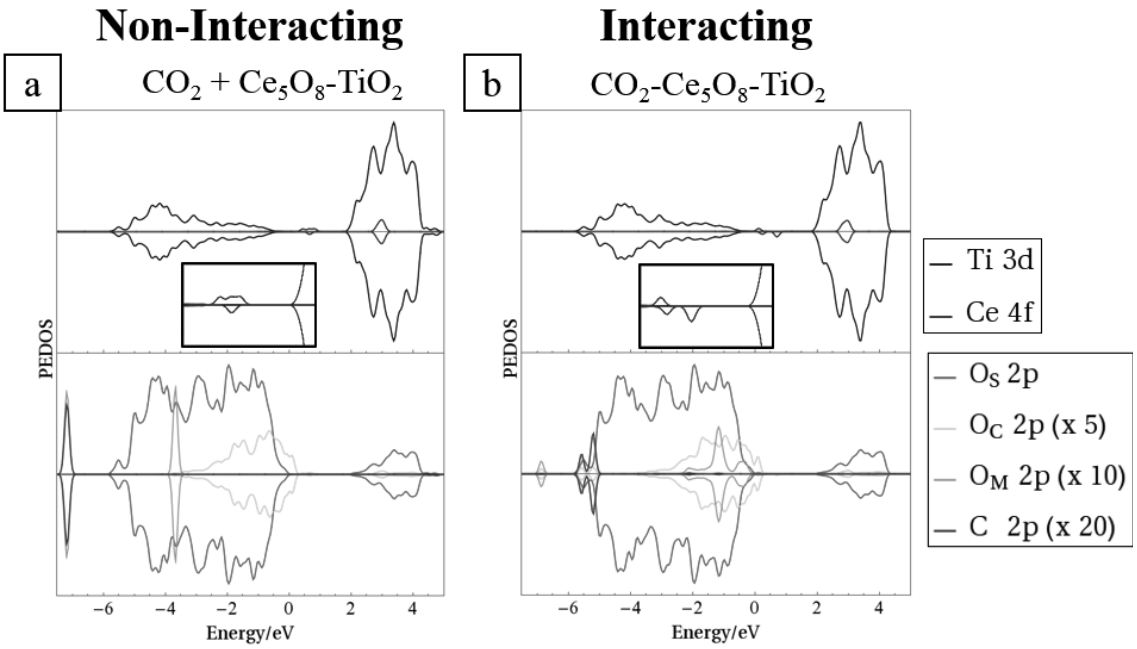

Figure 8. Spin polarized projected electron density of states (PEDOS) for **(a)** CO_2 + Ce_5O_8-rutile-(110) (non-interacting) and **(b)** CO_2-Ce_5O_8-rutile-(110) (interacting). The top half of each panel displays Ti 3d- and Ce 4f-derived states. Bottom halves of the panels display contributions to the DOS from surface (O_S), nanocluster (O_C) and CO2 molecule (O_M) oxygen 2p-derived states and H 1s states**.** Insets in the top panels show the mid-gap Ce-derived states in the range [-0.25 eV, +2.25 eV].

For the interacting case (Figure 8(b)), the O_M 2p-derived states overlap the O_C 2p-derived states near the VBM. The interaction increases the gap between the occupied Ce 4f-derived states and the CBM of the TiO_2 host; i.e. the occupied Ce^{3+} states are pushed to lower energy after interaction. Integrating the O_C and O_M-derived DOS lying above the TiO_2 VBM in both the non-interacting and interacting cases shows that after interaction the occupied states are driven to lower energies. The interaction of CO_2 at the reduced composite surfaces passivates high-lying electronic states; fewer O 2p-derived states appear above the VBM and occupied Ce states in the bandgap are pushed to lower energies.

In addition, the presence of low coordinated Ce cation sites in the supported nanoclusters can further facilitate the interaction with CO_2 in which under-coordinated Ce sites form new Ce-O bonds with oxygen from the molecule; the resulting Ce-O distances are consistent with typical Ce-O distances in reduced CeO_2. The presence of reduced Ce in off-stoichiometric supported CeO_x means that there are high-lying Ce^{3+} states and this charge accumulation on Ce can also promote the interaction with CO_2.

4 CONCLUSIONS

We have studied rutile TiO_2 (110) modified with ceria nanoclusters of compositions Ce_5O_{10} and Ce_6O_{12} using first principles DFT+U analysis. Our results show that the ground state of the nanocluster-surface composites is off-stoichiometric with one or more oxygen vacancies forming spontaneously or at very low energy cost, so that under typical experimental conditions, there will be oxygen vacancies present. As a consequence, Ce^{3+} ions will be present in the nanoclusters in their ground state (with no Ti^{3+} species) and occupied Ce 4f-derived states emerge in the TiO_2-derived bandgap. Together with O 2p states above the TiO_2 VB, due to low-coordinated oxygen atoms in the supported nanoclusters, this may induce a red shift in light absorption making these systems visible light active.

The photoexcited state model, shows that electron and hole localization occur at Ce and low-coordinated O_C sites respectively. The consequence of this for charge recombination may not be detrimental as the electron-hole pair has a large trapping energy of 0.8 eV so this can reduce the migration of charges over the nanocluster. Verification of both the predicted red shift and the charge recombination effects would be welcome.

In terms of activity, the CeO_2-rutile composites are more reducible compared to unmodified rutile (110) and moderate energy inputs are required to produce multiple oxygen vacancies.

Electrons released after oxygen vacancy formation localize on Ce sites in the supported nanoclusters.

The interaction of H_2O at the reduced ceria-modified rutile composites was investigated. This is important for a number of reactions, such as water gas shift or water oxidation and one of the limiting steps in these reactions is water dissociation which usually has an energy cost and an activation barrier. On both reduced ceria-TiO_2 systems, water adsorption is exothermic and favourable and, importantly, this leads to spontaneous dissociation of water to form surface bound hydroxyls.

Finally, CO_2 adsorption is favourable at multiple sites on the nanocluster-modified surface, with exothermic adsorption energies up to 1.25 eV. This strong adsorption is accompanied by a distortion from the linear gas phase CO_2 geometry, in which the molecule bends, with O-C-O angles of 125°-128°, and the C-O bonds in CO_2 show an elongation of ~0.10 Å. In combination with some transfer of charge between the adsorbed species and the nanocluster, this suggests the formation of activated CO_2, which is the crucial first step in the transformation of CO_2 to more useful molecules. We welcome attempts to study these materials for their ability to activate and convert CO_2, although the actual conversion process may be limited by other factors. Nevertheless, the finding that these ceria-modified TiO_2 systems can activate CO_2 is a promising first step.

The results of this paper show that ceria-modified rutile TiO_2 composites can (1) have reduced Ce^{3+} cations, (2) show red shift in light absorption, (3) adsorb and activate carbon dioxide and (4) adsorb and activate water. This makes these composites interesting materials for the activation and conversion of CO_2 and water.

ACKNOWLEDGEMENTS

Financial Support from Science Foundation Ireland through the Starting Investigator Research Grant Project EMOIN SFI/SIRG/09/I2160, the Science Foundation Ireland US-Ireland R&D Partnership Program Project SusChem SFI/US/14/E2915 and the ERA.Net for Materials Research and Innovation (M-ERA.Net 2), Horizon 2020 grant agreement number 685451, Science Foundation Ireland, Ireland, Grant Number SFI/16/M-ERA/3418 RATOCAT is gratefully acknowledged. Access to the computational resources at the Science Foundation Ireland/Higher Education Authority funded Irish Center for High End Computing is acknowledged. We are grateful for support from the COST Action CM1104 "Reducible Metal Oxides, Structure and Function". We acknowledge important discussions with Profs. K. A. Gray, E. Weitz and J. A. Byrne.

REFERENCES

1. A. Fujishima and K. Honda, *Nature*, 1972, **238**, 37-38.
2. C. Di Valentin, E. Finazzi, G. Pacchioni, A. Selloni, S. Livraghi, M. C. Paganini and E. Giamello, *Chem. Phys.*, 2007, **339**, 44-56.
3. X. Nie, S. Zhuo, G. Maeng and K. Sohlberg, *Int. J. Photoenergy*, 2009, **2009**, 22.
4. K. Yang, Y. Dai, B. Huang and M.-H. Whangbo, *J. Phys. Chem. C*, 2009, **113**, 2624-2629.
5. J. Yu, Q. Xiang and M. Zhou, *Appl. Catal., B*, 2009, **90**, 595-602.
6. J. W. Zheng, A. Bhattcahrayya, P. Wu, Z. Chen, J. Highfield, Z. Dong and R. Xu, *J. Phys. Chem. C*, 2010, **114**, 7063-7069.
7. A. M. Czoska, S. Livraghi, M. Chiesa, E. Giamello, S. Agnoli, G. Granozzi, E. Finazzi, C. D. Valentin and G. Pacchioni, *J. Phys. Chem. C*, 2008, **112**, 8951-8956.
8. P. Haowei, L. Jingbo, L. Shu-Shen and X. Jian-Bai, *J. Phys.: Condens. Matter*, 2008, **20**, 125207.
9. J.-M. Herrmann, *New J. Chem.*, 2012, **36**, 883-890.
10. T. Ikeda, T. Nomoto, K. Eda, Y. Mizutani, H. Kato, A. Kudo and H. Onishi, *J. Phys. Chem. C*, 2008, **112**, 1167-1173.
11. J.-P. Xu, L. Li, L.-Y. Lv, X.-S. Zhang, X.-M. Chen, J.-F. Wang, F.-M. Zhang, W. Zhong and Y.-W. Du, *Chin. Phys. Lett.*, 2009, **26**, 097502.
12. W. Li, *Phys. Status Solidi RRL*, 2015, **9**, 10-27.
13. V. Etacheri, C. Di Valentin, J. Schneider, D. Bahnemann and S. C. Pillai, *J. Photochem. Photobiol. C: Photochem. Rev.*, 2015, **25**, 1-29.
14. S. Na Phattalung, S. Limpijumnong and J. Yu, *Appl. Catal., B*, 2017, **200**, 1-9.
15. C. D. Valentin, G. Pacchioni, H. Onishi and A. Kudo, *Chem. Phys. Lett.*, 2009, **469**, 166-171.
16. Y. Gai, J. Li, S. S. Li, J. B. Xia and S. H. Wei, *Phys. Rev. Lett.*, 2009, **102**, 036402.
17. R. Long and N. J. English, *J. Phys. Chem. C*, 2010, **114**, 11984-11990.

18. R. Long and N. J. English, *Chem. Mater.*, 2010, **22**, 1616-1623.
19. J. Zhang, C. Pan, P. Fang, J. Wei and R. Xiong, *ACS Appl. Mater. Interfaces*, 2010, **2**, 1173-1176.
20. W. Zhu, X. Qiu, V. Iancu, X.-Q. Chen, H. Pan, W. Wang, N. M. Dimitrijevic, T. Rajh, H. M. Meyer, M. P. Paranthaman, G. M. Stocks, H. H. Weitering, B. Gu, G. Eres and Z. Zhang, *Phys. Rev. Lett.*, 2009, **103**, 226401.
21. M. Grätzel, *J. Photochem. Photobiol. C: Photochem. Rev.*, 2003, **4**, 145-153.
22. W. Hou and S. B. Cronin, *Adv. Funct. Mater.*, 2013, **23**, 1612-1619.
23. M. Honda, Y. Kumamoto, A. Taguchi, Y. Saito and S. Kawata, *Appl. Phys. Lett.*, 2014, **104**, 061108.
24. S. Shuang, R. Lv, Z. Xie and Z. Zhang, *Sci. Rep.*, 2016, **6**, 26670.
25. S. Linic, P. Christopher and D. B. Ingram, *Nat. Mater.*, 2011, **10**, 911.
26. S. C. Warren and E. Thimsen, *Energy Environ Sci.*, 2012, **5**, 5133-5146.
27. Q. Jin, M. Fujishima and H. Tada, *J. Phys. Chem. C*, 2011, **115**, 6478-6483.
28. H. Tada, Q. Jin, A. Iwaszuk and M. Nolan, *J. Phys. Chem. C*, 2014, **118**, 12077-12086.
29. J. A. Libera, J. W. Elam, N. F. Sather, T. Rajh and N. M. Dimitrijevic, *Chem. Mater.*, 2010, **22**, 409-413.
30. M. Nolan, *Phys. Chem. Chem. Phys.*, 2011, **13**, 18194-18199.
31. M. Fronzi, W. Daly and M. Nolan, *Appl. Catal., A:* , 2016, **521**, 240-249.
32. M. Nolan, A. Iwaszuk, A. K. Lucid, J. J. Carey and M. Fronzi, *Adv. Mater.*, 2016, **28**, 5425-5446.
33. M. Fronzi, A. Iwaszuk, A. Lucid and M. Nolan, *J. Phys.: Condens. Matter*, 2016, **28**, 074006.
34. M. Nolan, A. Iwaszuk and K. A. Gray, *J. Phys. Chem. C*, 2014, **118**, 27890-27900.
35. A. Lucid, A. Iwaszuk and M. Nolan, *Mater. Sci. Semicond. Process.*, 2014, **25**, 59-67.
36. A. Iwaszuk and M. Nolan, *Catal. Sci. Technol.*, 2013, **3**, 2000-2008.
37. A. Iwaszuk and M. Nolan, *J. Mater. Chem. A*, 2013, **1**, 6670-6677.
38. A. Iwaszuk, P. A. Mulheran and M. Nolan, *J. Mater. Chem. A*, 2013, **1**, 2515-2525.
39. A. Iwaszuk, M. Nolan, Q. Jin, M. Fujishima and H. Tada, *J. Phys. Chem. C*, 2013, **117**, 2709-2718.
40. M. Nolan, *ACS Appl. Mater. Interfaces*, 2012, **4**, 5863-5871.
41. M. Nolan, *Chem. Commun.*, 2011, **47**, 8617-8619.
42. J. B. Park, J. Graciani, J. Evans, D. Stacchiola, S. D. Senanayake, L. Barrio, P. Liu, J. F. Sanz, J. Hrbek and J. A. Rodriguez, *J. Am. Chem. Soc.*, 2010, **132**, 356-363.
43. A. Iwaszuk and M. Nolan, *Phys. Chem. Chem. Phys.*, 2011, **13**, 4963-4973.
44. S. J. A. Moniz, S. A. Shevlin, X. An, Z.-X. Guo and J. Tang, *Chem. Eur. J.*, 2014, **20**, 15571-15579.
45. Q. Jin, M. Fujishima, M. Nolan, A. Iwaszuk and H. Tada, *J. Phys. Chem. C*, 2012, **116**, 12621-12626.
46. Y.-F. Li and Z.-P. Liu, *Wiley Interdiscip. Rev. Comput. Mol. Sci.*, 2016, **6**, 47-64.
47. Y. Cheng and S. P. Jiang, *Prog. Nat. Sci. Mater. Int.*, 2015, **25**, 545-553.
48. Á. Valdés, Z. W. Qu, G. J. Kroes, J. Rossmeisl and J. K. Nørskov, *J. Phys. Chem. C*, 2008, **112**, 9872-9879.
49. A. V. Bandura, D. G. Sykes, V. Shapovalov, T. N. Troung, J. D. Kubicki and R. A. Evarestov, *J. Phys. Chem. B*, 2004, **108**, 7844-7853.
50. D. Fernández-Torre, K. Kośmider, J. Carrasco, M. V. Ganduglia-Pirovano and R. Pérez, *J. Phys. Chem. C*, 2012, **116**, 13584-13593.
51. M. Fronzi, S. Piccinin, B. Delley, E. Traversa and C. Stampfl, *Phys. Chem. Chem. Phys.*, 2009, **11**, 9188-9199.
52. H. Zhang, P. Zhou, Z. Chen, W. Song, H. Ji, W. Ma, C. Chen and J. Zhao, *J. Phys. Chem. C*, 2017, **121**, 2251-2257.
53. C. Sun, L.-M. Liu, A. Selloni, G. Q. Lu and S. C. Smith, *J. Mater. Chem.*, 2010, **20**, 10319-10334.
54. Y.-F. Li and A. Selloni, *ACS Catal.*, 2016, **6**, 4769-4774.
55. N. Tymińska, G. Wu and M. Dupuis, *J. Phys. Chem. C*, 2017, **121**, 8378-8389.
56. M.-T. Nguyen, S. Piccinin, N. Seriani and R. Gebauer, *ACS Catal.*, 2015, **5**, 715-721.

57. J. Graciani, J. J. Plata, J. F. Sanz, P. Liu and J. A. Rodriguez, *J. Chem. Phys.*, 2010, **132**, 104703.
58. J. Cheng, J. VandeVondele and M. Sprik, *J. Phys. Chem. C*, 2014, **118**, 5437-5444.
59. D. Wang, H. Wang and P. Hu, *Phys. Chem. Chem. Phys.*, 2015, **17**, 1549-1555.
60. X. Chen, S. N. Choing, D. J. Aschaffenburg, C. D. Pemmaraju, D. Prendergast and T. Cuk, *J. Am. Chem. Soc.*, 2017, **139**, 1830-1841.
61. X. Chang, T. Wang and J. Gong, *Energy Environ Sci.*, 2016, **9**, 2177-2196.
62. V. P. Indrakanti, *Fuel Process. Technol.*, 2011, **v. 92**, pp. 805-811-2011 v.2092 no.2014.
63. W. Pipornpong, R. Wanbayor and V. Ruangpornvisuti, *Appl. Surf. Sci.*, 2011, **257**, 10322-10328.
64. W.-J. Yin, B. Wen, S. Bandaru, M. Krack, M. W. Lau and L.-M. Liu, *Sci. Rep.*, 2016, **6**, 23298.
65. C.-T. Yang, B. C. Wood, V. R. Bhethanabotla and B. Joseph, *J. Phys. Chem. C*, 2014, **118**, 26236-26248.
66. R. J. Walker, A. Pougin, F. E. Oropeza, I. J. Villar-Garcia, M. P. Ryan, J. Strunk and D. J. Payne, *Chem. Mater.*, 2016, **28**, 90-96.
67. E. L. Uzunova, N. Seriani and H. Mikosch, *Phys. Chem. Chem. Phys.*, 2015, **17**, 11088-11094.
68. A. K. Mishra, A. Roldan and N. H. d. Leeuw, *J. Chem. Phys.*, 2016, **145**, 044709.
69. A. K. Mishra, A. Roldan and N. H. de Leeuw, *J. Phys. Chem. C*, 2016, **120**, 2198-2214.
70. H. Wu, N. Zhang, H. Wang and S. Hong, *Chem. Phys. Lett.*, 2013, **568**, 84-89.
71. L. I. Bendavid and E. A. Carter, *J. Phys. Chem. C*, 2013, **117**, 26048-26059.
72. H. Wu, N. Zhang, Z. Cao, H. Wang and S. Hong, *Int. J. Quantum Chem*, 2012, **112**, 2532-2540.
73. J. Graciani, K. Mudiyanselage, F. Xu, A. E. Baber, J. Evans, S. D. Senanayake, D. J. Stacchiola, P. Liu, J. Hrbek, J. F. Sanz and J. A. Rodriguez, *Science*, 2014, **345**, 546-550.
74. M. Behrens, F. Studt, I. Kasatkin, S. Kühl, M. Hävecker, F. Abild-Pedersen, S. Zander, F. Girgsdies, P. Kurr, B.-L. Kniep, M. Tovar, R. W. Fischer, J. K. Nørskov and R. Schlögl, *Science*, 2012, **336**, 893-897.
75. W. J. Durand, A. A. Peterson, F. Studt, F. Abild-Pedersen and J. K. Nørskov, *Surf. Sci.*, 2011, **605**, 1354-1359.
76. L. C. Grabow and M. Mavrikakis, *ACS Catal.*, 2011, **1**, 365-384.
77. Y. Wang, J. Zhao, T. Wang, Y. Li, X. Li, J. Yin and C. Wang, *J. Catal.*, 2016, **337**, 293-302.
78. J. B. Park, J. Graciani, J. Evans, D. Stacchiola, S. Ma, P. Liu, A. Nambu, J. F. Sanz, J. Hrbek and J. A. Rodriguez, *Proc. Natl. Acad. Sci. U.S.A.*, 2009, **106**, 4975-4980.
79. A. C. Johnston-Peck, S. D. Senanayake, J. J. Plata, S. Kundu, W. Xu, L. Barrio, J. Graciani, J. F. Sanz, R. M. Navarro, J. L. G. Fierro, E. A. Stach and J. A. Rodriguez, *J. Phys. Chem. C*, 2013, **117**, 14463-14471.
80. C. L. Muhich, B. D. Ehrhart, I. Al-Shankiti, B. J. Ward, C. B. Musgrave and A. W. Weimer, *Wiley Interdisciplinary Reviews: Energy and Environment*, 2016, **5**, 261-287.
81. G. Kresse and J. Hafner, *Phys. Rev. B.*, 1994, **49**, 14251-14269.
82. J. Furthmüller, J. Hafner and G. Kresse, *Phys. Rev. B.*, 1996, **53**, 7334-7351.
83. P. E. Blöchl, *Phys. Rev. B.*, 1994, **50**, 17953-17979.
84. G. Kresse and D. Joubert, *Phys. Rev. B.*, 1999, **59**, 1758-1775.
85. J. P. Perdew, K. Burke and M. Ernzerhof, *Phys. Rev. Lett.*, 1996, **77**, 3865-3868.
86. V. I. Anisimov, J. Zaanen and O. K. Andersen, *Phys. Rev. B.*, 1991, **44**, 943-954.
87. S. L. Dudarev, G. A. Botton, S. Y. Savrasov, C. J. Humphreys and A. P. Sutton, *Phys. Rev. B.*, 1998, **57**, 1505-1509.
88. B. J. Morgan and G. W. Watson, *Surf. Sci.*, 2007, **601**, 5034-5041.
89. D. A. Andersson, S. I. Simak, B. Johansson, I. A. Abrikosov and N. V. Skorodumova, *Phys. Rev. B.*, 2007, **75**, 035109.
90. H. P. Boehm, *Discuss. Faraday Soc.*, 1971, **52**, 264-275.
91. G. E. Brown, V. E. Henrich, W. H. Casey, D. L. Clark, C. Eggleston, A. Felmy, D. W. Goodman, M. Grätzel, G. Maciel, M. I. McCarthy, K. H. Nealson, D. A. Sverjensky, M. F. Toney and J. M. Zachara, *Chem. Rev.*, 1999, **99**, 77-174.
92. M. Fronzi and M. Nolan, *ACS Omega*, 2017, **2**, 6795-6808.
93. G. Henkelman, A. Arnaldsson and H. Jónsson, *Comput. Mater. Sci.*, 2006, **36**, 354-360.
94. C. Di Valentin and A. Selloni, *J. Phys. Chem. Lett.*, 2011, **2**, 2223-2228.
95. A. Iwaszuk and M. Nolan, *J. Phys. Chem. C*, 2011, **115**, 12995-13007.

96. A. R. Albuquerque, A. Bruix, I. M. G. dos Santos, J. R. Sambrano and F. Illas, *J. Phys. Chem. C*, 2014, **118**, 9677-9689.
97. A. R. Albuquerque, A. Bruix, J. R. Sambrano and F. Illas, *J. Phys. Chem. C*, 2015, **119**, 4805-4816.
98. J. B. Park, J. Graciani, J. Evans, D. Stacchiola, S. D. Senanayake, L. Barrio, P. Liu, J. F. Sanz, J. Hrbek and J. A. Rodriguez, *J. Am. Chem. Soc.*, 2009, **132**, 356-363.
99. Z. Yang, L. Xie, D. Ma and G. Wang, *J. Phys. Chem. C*, 2011, **115**, 6730-6740.
100. S. Fuente, M. M. Branda and F. Illas, *Theor. Chem. Acc.*, 2012, **131**, 1190.
101. M. Molinari, S. C. Parker, D. C. Sayle and M. S. Islam, *J. Phys. Chem. C*, 2012, **116**, 7073-7082.
102. D. Marrocchelli and B. Yildiz, *J. Phys. Chem. C*, 2012, **116**, 2411-2424.
103. D. R. Mullins, P. M. Albrecht, T.-L. Chen, F. C. Calaza, M. D. Biegalski, H. M. Christen and S. H. Overbury, *J. Phys. Chem. C*, 2012, **116**, 19419-19428.
104. J. Carrasco, D. López-Durán, Z. Liu, T. Duchoň, J. Evans, S. D. Senanayake, E. J. Crumlin, V. Matolín, J. A. Rodríguez and M. V. Ganduglia-Pirovano, *Angew. Chem. Int. Ed.*, 2015, **54**, 3917-3921.
105. J. Fan, B. Xu, J. Z. Zhao and H. Xu, *Phys. Chem. Chem. Phys.*, 2018, **20**, 1575-1582.
106. J. Gan, X. Lu, J. Wu, S. Xie, T. Zhai, M. Yu, Z. Zhang, Y. Mao, S. C. I. Wang, Y. Shen and Y. Tong, *Sci. Rep.*,2013, **3**, 1021.
107. L. Liu, C. Zhao and Y. Li, *J. Phys. Chem. C*, 2012, **116**, 7904-7912.
108. Y.-X. Pan, Z.-Q. Sun, H.-P. Cong, Y.-L. Men, S. Xin, J. Song and S.-H. Yu, *Nano Res.*, 2016, **9**, 1689-1700.
109. S. Huygh, A. Bogaerts and E. C. Neyts, *J. Phys. Chem. C*, 2016, **120**, 21659-21669.
110. Z. Cheng, B. J. Sherman and C. S. Lo, *J. Chem. Phys.*, 2013, **138**, 014702.
111. X. Lu, W. Wang, S. Wei, C. Guo, Y. Shao, M. Zhang, Z. Deng, H. Zhu and W. Guo, *RSC Adv.*, 2015, **5**, 97528-97535.
112. A. B. Vidal, L. Feria, J. Evans, Y. Takahashi, P. Liu, K. Nakamura, F. Illas and J. A. Rodriguez, *J. Phys. Chem. Lett.*, 2012, **3**, 2275-2280.
113. S. Posada-Perez, F. Vines, P. J. Ramirez, A. B. Vidal, J. A. Rodriguez and F. Illas, *Phys. Chem. Chem. Phys.*, 2014, **16**, 14912-14921.
114. C. Liu, T. R. Cundari and A. K. Wilson, *J. Phys. Chem. C*, 2012, **116**, 5681-5688.
115. Z. Wu, A. K. P. Mann, M. Li and S. H. Overbury, *J. Phys. Chem. C*, 2015, **119**, 7340-7350.

CO_2 and Water Activation on Ceria Nanocluster Modified TiO_2 Rutile (110)

Stephen Rhatigan and Michael Nolan

Ceria nanocluster modification of TiO_2 rutile (110): Ce^{3+} formation, reduced energy gap, and enhanced CO_2 and water activation.